Further calibration and validation of FLORIS with wind tunnel data

Filippo Campagnolo, Lejla Imširović, Robert Braunbehrens and Carlo L. Bottasso

Wind Energy Institute, Technische Universität München, Boltzmannstraße 15, D-85748 Garching bei München, Germany

E-mail: filippo.campagnolo@tum.de

Abstract. This paper compares the accuracy of four different FLORIS model implementations characterized by increasing levels of accounted physics. The predictions of each model were tested against experimental observations obtained from wind tunnel tests of a cluster of three scaled wind turbines. The experiments were conducted for a wide range of environmental conditions, and mainly with yawed turbines. The results showed a significant improvement in the accuracy of the base model by adding more details to the physical effects of the simulation, such as secondary steering and a heterogeneous flow field. It is also interesting to note that the FLORIS predictions become particularly accurate when considering inflow-dependent power losses in yaw-misaligned conditions.

1. Introduction

In recent years there has been a considerable progress in the development of control strategies capable of increasing the overall power produced by wind farms. One of the most promising technologies is wake steering by yawing, whose potential has been demonstrated both in simulated environments [1], as well as in wind tunnels [2] and through field experiments [3–5]. In all the above mentioned experimental campaigns, this control strategy has been implemented in open-loop by means of precomputed Look-Up Tables (LUTs), which store the desired optimal misalignment as a function of the main features of the atmospheric flow such as wind speed, direction, and turbulence. The LUTs are generally obtained offline by solving optimum problems applied to wind farm engineering models, whose level of fidelity to reality can have a considerable impact on the achievable gain [6]. One of the most widely used models is FLORIS [7], which features a plethora of wake and turbulence submodels. It also allows accounting for spatially heterogeneous inflows. Despite quite some work has been done in comparing FLORIS predictions against SCADA and flow measurements [8,9], the need of further validation has been advocated by the research community [10].

This paper, therefore, aims at further validating FLORIS and its submodels through the use of accurate and extensive wind tunnel dataset. Specifically, this paper expands on the work conducted by [11], thus extending the inflow conditions and models features for which validation was performed in that work. In this regard, a cluster of three scaled wind turbine models (named G1 [12]) has been tested under a wide range of inflow and misaligned operating conditions, and the measured physical quantities have been compared to FLORIS predictions.

Recent findings [13] concluded that the wake emitted by the G1 is remarkably similar to the one of a reference full-scale wind turbine, which reasonably allows saying that the results achieved in this work can also provide indications on the behavior of FLORIS at full-scale.

The paper is organized as follows. First, the experimental setup is presented in Sec. 2, followed by the description of the four simulated FLORIS implementations in Sec. 3. The dedicated tuning process used for the calibration of the free parameters of each model is then presented in Sec. 4, while the comparison between the predictions of the model and the experimental observations is given in Sec. 5. Lastly, the concluding remarks are given in Sec. 6.

2. Experimental setup

2.1. Scaled cluster

The scaled cluster is the one described in [2], and is depicted in Figure 1. It is composed of three fully sensorized, scaled G1 wind turbines installed on the 13 m diameter turntable of the atmospheric test section of the wind tunnel of the Politecnico di Milano.

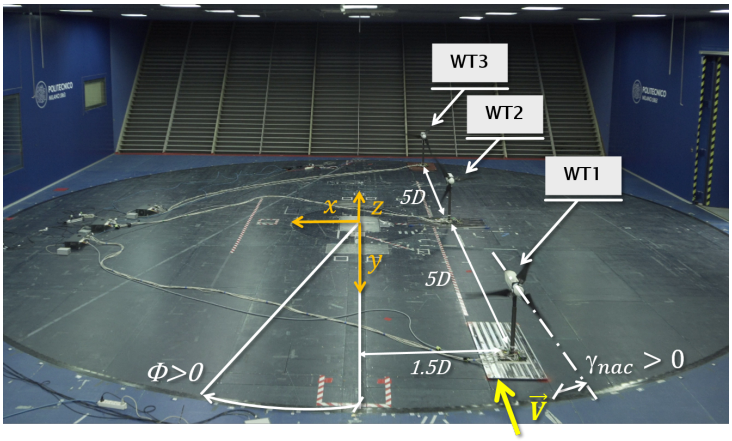

Figure 1: Experimental setup, showing the three model turbines mounted on the wind tunnel turntable. The x–y–z frame is fixed with respect to the tunnel and does not rotate with the turntable, while the z-axis pointing towards the ceiling (Figure reproduced from [2]).

The pitch and generator torque of the G1s are regulated by a standard power controller. The machines can furthermore operate misaligned with respect to the incoming flow direction of an angle γ, defined positive for a counterclockwise misalignment viewed from the top. Each G1 is equipped with a rotor whose diameter D is equal to 1.1 m, while the hub height z_{H} is 0.825 m.

Figure 2a reports the relationship between the G1 rotor power coefficient C_{P} and the rotor-effective wind speed U_{REWS}, which clearly shows that the G1 energy extraction process in region II (i.e. for wind speeds lower than approximately 5.7 m/s) is affected by the Reynolds-dependency of its airfoil polars [14]. while in region III the power coefficient decreases as the collective blade pitch is increased. At low winds, and hence at low rotational speeds, the blade airfoil efficiency is reduced because of the low chord-based Reynolds number, resulting in a reduction of C_{P}. Figure 2b, instead, depicts the behavior of C_{P} with respect to the misalignment angle γ, which was characterized with dedicated wind tunnel tests conducted at wind speeds in the range of 5-5.7 m/s. The same figure also includes the best fitting cosine-law power-loss exponents, equal to 2.174. For further features about the G1s, the reader is referred to [2] and [12].

Concerning the scaled cluster, WT1 (upstream), WT2 (center), and WT3 (downstream) turbines are longitudinally spaced 5D and located 1.5D aside of the center-line of the turntable.

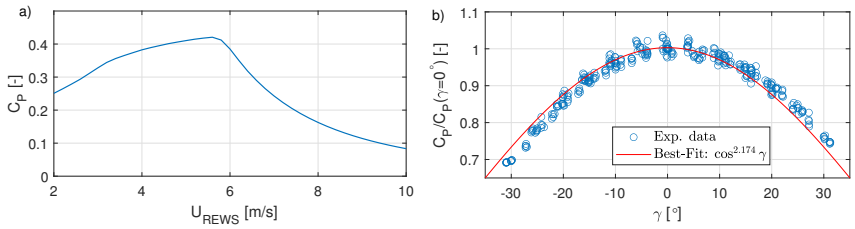

Figure 2: C_P vs. rotor-equivalent wind speed (a) and vs. misalignment angle γ (b).

This last can be rotated by the angle Φ to simulate different wind directions; Φ is zero when the turbine row is parallel to the wind tunnel center-line, while it is positive for a clockwise rotation of the turntable, if viewed from the top as shown in Figure 1.

2.2. Wind tunnel inflow

During the experiment, the ambient wind speed U_{Pitot} was measured by a Pitot tube located outside the turntable, 1.5D aside of the center-line of the turntable, 3D upwind of WT1 and at hub height. Two boundary layers, characterized by moderate (mod-TI) and high (high-TI) turbulent inflows, were instead simulated by placing roughness element on the floor and turbulence generators at the chamber inlet. The resulting inflow was measured with three-component constant temperature hot-wire probes (CTA), scanning a vertical plane 4D upwind of WT1. The corresponding speed mappings, normalized with respect to the inflow speed measured at the Pitot tube location, are depicted in Figure 3(a) and (b). The vertical profiles of the normalized wind speed measured at the Pitot location are instead shown in Figure 3(c) on the left, together with their best fitting power-laws. Finally, the vertical profiles of the turbulence intensity are shown in Figure 3(c) on the right. Figures 3(a) and (b), particularly, highlight the high non-homogeneity of the inflow, both horizontally and vertically. The variability along the vertical axis can be ascribed to the vertical shear. The variability along the horizontal axis, instead, is due to the non-uniformity of the inflow speed at the chamber inlet, which is in turn affected by the non-homogeneous distribution of structural elements placed before and immediately after the chamber inlet. Among the former are the heat exchanger, the fans support structures and the uprights of the mesh used to dissipate the turbulent structures. For the latter, however, it is mainly the trapezoidal spires used as turbulence generators.

2.3. Experimental data

The tests were conducted at a constant average wind speed equal to approx. 5.6 and 5.3 m/s, respectively when testing with mod-TI and high-TI. For both simulated turbulent inflows, tests were conducted with 11 wind directions $\Phi = [0, \pm 2.29, \pm 4.58, \pm 6.89, \pm 9.21, \pm 11.54]^\circ$. Figure 4 reports, for each of the considered wind direction, the tested combinations of steady misalignment angles for WT1 (γ_1) and WT2 (γ_2). This resulted in a unique and wide dataset comprising 622 different operating conditions. Among the available measurements are the 2-min average power produced by each wind turbine within the cluster. Together with the average wind speeds measured by the Pitot tube, the turntable angle and the inflow turbulence, the power data are the only measurements used in this work.

3. FLORIS

FLORIS (FLOw Redirection and Induction in Steady State) [15] is an open-source framework developed by the National Renewable Energy Laboratory (NREL) in collaboration with TU Delft for real-time wind farm control, low-fidelity wind farm analysis, and layout optimization.

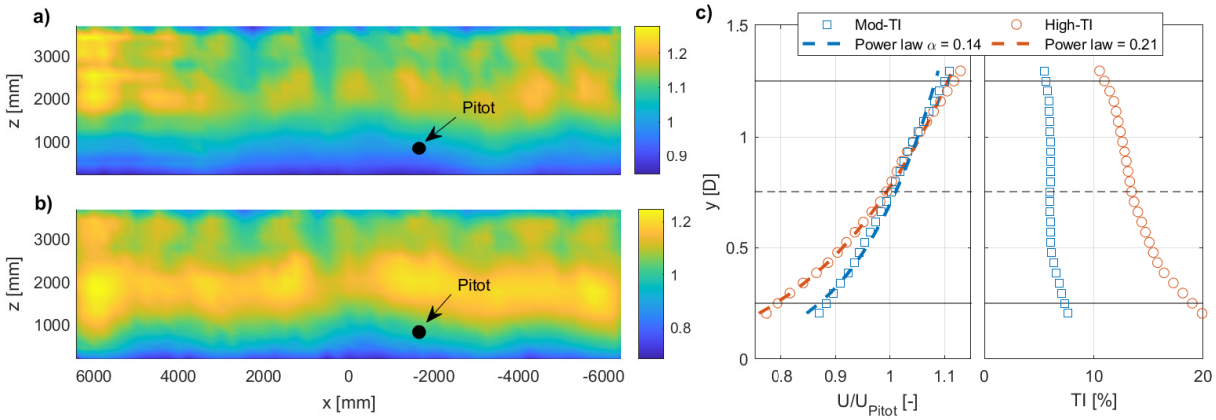

Figure 3: Characteristics of the inflows simulated within the wind tunnel and measured by the CTA probes: normalized wind velocity for mod-TI (a) and high-TI (b); vertical profiles of the normalized wind speed and their best fitting power-law exponent α (c, left); vertical profiles of the turbulence intensity (c, right); within (c), the black-dashed line indicates the hub height, while the two solid black lines limit the rotor disk.

Since it was released, FLORIS has been under continuous development, with a stable 2.3 version of the code available at GitHub (GitHub link). The model is equipped with a set of control-oriented wake and turbine submodels, as well as tools for the development and analysis of wake control strategies [16].

Built in a modular way, it allows the user to work with multiple implementations which differ depending on the submodels selected for the modelling of the wake speed and deflection, of the wake-added turbulence, and of the wakes superposition.

The interaction between the turbine and the wind flow is modeled according to FLORIS' wind turbine model, which schedules the power (C_P) and thrust (C_T) coefficients as function of the rotor effective wind speed U_REWS. Additionally, FLORIS employs an expression for the steady-state power of a yawed turbine according to [17], which is given by equation 1.

$$P\left(U_\mathrm{REWS}, \gamma\right) = \frac{1}{2}\rho A C_\mathrm{P} \left(\cos\gamma\right)^{p_\mathrm{P}} U_\mathrm{REWS}^3 \tag{1}$$

Here, the cosine exponent p_P is a tunable parameter that quantifies the power loss due to yaw misalignment. A similar equation is employed to model the impact of yawed operations on the thrust coefficient.

3.1. Wake-added turbulence submodel

Two submodels for the wake-added turbulence were initially considered in this work: the Crespo-Hernández [18] and the Ishihara-Qian [19]. An initial investigation showed that the Ishihara-Qian submodel leads to a better match with the measured power outputs. It has been therefore adopted in all the implementations of FLORIS described in the following section.

A modification was additionally applied to the part of FLORIS source code that calculates the wake-added turbulence sensed by a downstream turbine. The built-in method, based on [20], estimates this quantity as follows. It samples the model predicted wake-added turbulence at the rotor apex of a downstream turbine, and multiplies the resulting value with the ratio between the wake-overlap and the rotor disk areas. As the Crespo-Hernández and Ishiahara-Qian submodels approximate the wake-added turbulence with top-hat and double-Gaussian functions, respectively, the predicted value is therefore a proper estimation of the average of

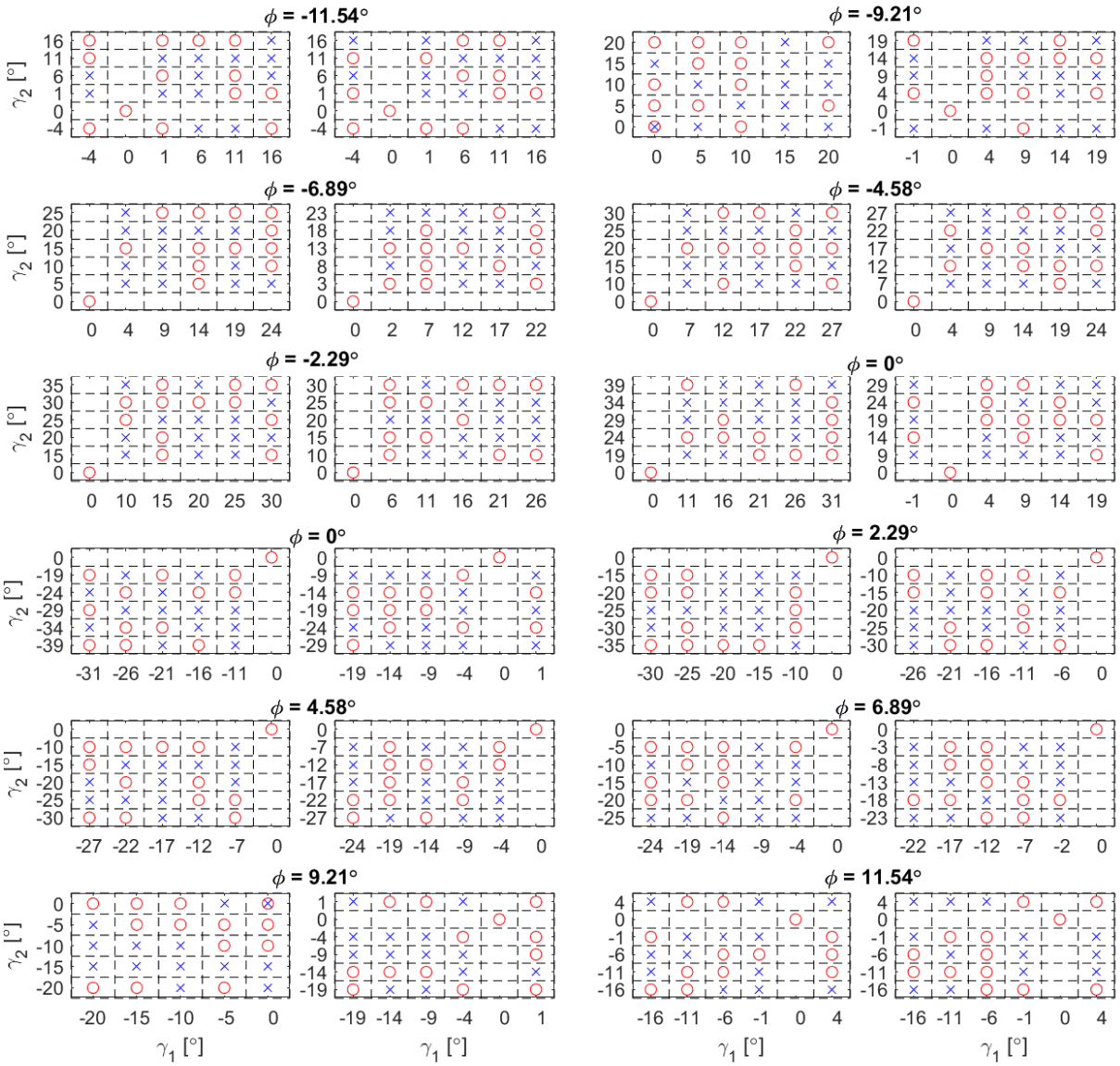

Figure 4: Tested combinations of steady misalignment angles for WT1 (γ_1) and WT2 (γ_2). Each cluster of two subplots represents a unique wind direction, as indicated by the title. For each considered wind direction, combinations tested with mod-TI and high-TI inflows are reported on the left and right subplots, respectively. Red circles: conditions used for the parameters tuning. Blue cross symbols: conditions used for the validation.

the wake-added turbulence over the rotor disk only when using the Crespo-Hernández, but not when using the Ishiahara-Qian model.

The code was then modified as follows. The predicted wake-added turbulence was sampled at several points uniformly distributed over the whole area of the downstream rotor. The resulting average was then added in quadrature to the inflow turbulence so as to estimate the local turbulence.

3.2. FLORIS Implementations

With the aim of showing improved power predictions when accounting for more detailed flow physics, four different FLORIS implementations were investigated. These models are characterized by increasing levels of accounted physics: Gauss-Legacy with homogeneous inflow (GL), Gauss-Curl-Hybrid with homogeneous inflow (GCH), Gauss-Curl-Hybrid with heterogeneous inflow (HET-GCH), and Gauss-Curl-Hybrid with heterogeneous inflow and yaw-induced power losses modeled with an inflow-dependent cosine-law (HET-GCH+P_{P}).

3.2.1. GL The first implementation is based on the Gauss-Legacy wake submodel, which was firstly introduced in 2014 [21], and further improved as described in [20, 22–24]. In order to account for the shear-induced wake deflection [17], a correction δ_x has been applied to the deflection model trough the following Eq. 2

$$\delta_x(y) = b_d \left(y_0 - y\right), \tag{2}$$

with y_0 the turbine position along the longitudinal axis. Finally, the sum-of-squares (SOSFS) was used as superposition model.

3.2.2. GCH The second model is the Gauss-Curl-Hybrid [25], which was proposed as a computationally more efficient alternative to the Curl model [26]. The GCH model combines the features of the Gauss-Legacy model with an analytical approximation of the Curl model. It is therefore capable of capturing, among others, the effects of secondary steering [27] with a negligible impact on the computational efficiency.

3.2.3. HET-GCH The two previously described FLORIS implementations do not account for heterogeneous inflow conditions, which could be observed in the field due to wind farm blockage effects [28] or the surrounding orography and vegetation [11], as well as in a wind tunnel due to the non-uniformity of the inflow speed at the chamber inlet.

Following the method proposed in [11], a correction to the homogeneous inflow field is therefore parameterized in terms of shape functions and associated speed-up ($\mathbf{p}_{speed}$) nodal values. Given the observed lateral variability of the wind speed within the wind tunnel (see Fig. 3), four speed-up nodes $\mathbf{c}_{speed}$ were located at x = [-3.5; -2.15; -0.8; 0.55] m (which correspond to approximately [-3.18; -1.95; -0.73; 0.5] D) and upstream of the cluster (y = 6 m), as shown in Fig. 5. In addition, the resulting mesh was discretized for different turntable angles, thus introducing a dependency between the inflow speed distribution and the turntable position. Such an approach allows to account for a different impact of the scaled cluster blockage on the upstream inflow as a result of the variation of the cluster layout [28]. This approach, therefore, differs from the one applied in [11], where only the mod-TI sub-set of the wind tunnel data was used. Therein, indeed, it was assumed that the lateral non-homogeneity of the inflow was not affected by the cluster layout. As shown in Fig. 5, the novel approach proposed in this work results in 4 nodes for each of the 7 considered turntable angles ($\Phi = [0, \pm4, \pm8, \pm12]^\circ$).

Finally, as the mod-TI and high-TI inflows are characterized by different distributions of the wind speed (as shown in Fig. 3), two sets of speed-up nodes were used to model the mod-TI and

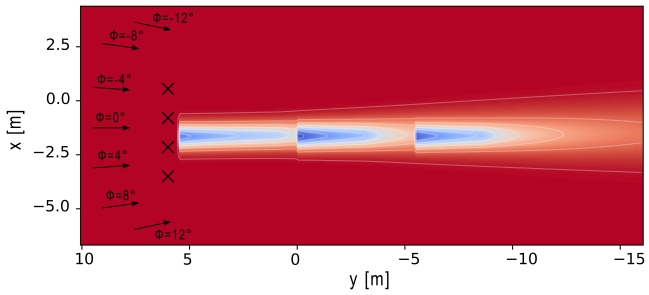

Figure 5: Distribution of the speed-up nodes within the simulated domain.

high-TI heterogeneous inflow fields, thus leading to a total of 56 nodes. Overall, the ambient wind speed has been parameterized as:

$$U_\infty\left(x, z, \phi, \mathrm{TI}_\infty\right) = U_{\mathrm{Pitot}}\left(\frac{z}{z_{\mathrm{H}}}\right)^{\alpha}\left[1 + f_{speed}\left(x, z, \phi, \mathrm{TI}_\infty, \mathbf{c}_{speed}, \mathbf{p}_{speed}\right)\right], \tag{3}$$

with TI_∞ the inflow turbulence at hub height, equal to 6.12% and 13% respectively for the mod-TI and high-TI inflows, and f_{speed} the interpolating bilinear shape function [11].

3.2.4. HET-GCH+P_{P} As previously mentioned, FLORIS calculates the power of a yawed turbine according to Eq. 1, where the cosine of the yaw angle is employed to account for the power reduction in yawed operations. Motivated by recent research results [29], it was decided to integrate the HET-GCH model with an inflow-speed dependency of the cosine exponent. In this regard, a linear relationship was assumed between the cosine exponent and U_{REWS}, thus resulting in the following equation:

$$p_{\mathrm{P}}\left(U_{\mathrm{REWS}}\right) = m_{\mathrm{P}} U_{\mathrm{REWS}} + k_{\mathrm{P}}, \tag{4}$$

where m_{P} and k_{P} are tunable parameters, which apply to all the turbines of the cluster.

4. Tuning parameters and process

The calibration parameters of the wake submodels, the speed-up nodal values as well as the coefficients of the relationship between the cosine exponent and U_{REWS}, are calibrated through a dedicated tuning process.

- All FLORIS implementations use the Bastankhah and Porté-Agel [21] wake velocity model. The parameters α, β, k_a, and k_b, as well as b_d of Eq. 2, are identified. All velocity model parameters are summarized in $\mathbf{p}_W$.
- The Ishihara-Qian turbulence submodel, also used by all implementations, consists of 15 calibration parameters. An initial investigation showed that only five of them had a significant effect on the model performance: k_{const}, $\epsilon_{\mathrm{const}}$, d_{const}, e_{const}, f_{const}. The parameters are stacked in $\mathbf{p}_T$.
- For the implementations HET-GCH and HET-GCH+P_{P}, the correction to the homogeneous inflow field is parameterized with $\mathbf{p}_{speed}$.
- HET-GCH+P_{P} includes additionally the coefficients m_p and k_p of Eq. 4, summarized in $\mathbf{p}_{yaw}$.

	Wake				Deflection	Wake-added Turbulence					P_{P}	
	α	β	k_a	k_b	b_d	k_{const}	$\epsilon_{\mathrm{const}}$	d_{const}	e_{const}	f_{const}	m_{P}	k_{P}
GL-default	0.58	0.077	0.384	0.0037	0.0	0.11	0.23	2.3	1.00	0.70	0.0	2.174
GL	0.61	0.084	0.274	0.0039	0.029	0.22	0.37	2.1	0.79	0.69	0.0	2.174
GCH	0.83	0.100	0.258	0.0036	0.028	0.08	0.19	3.4	2.00	0.72	0.0	2.174
HET-GCH	0.50	0.081	0.362	0.0043	0.024	0.12	0.26	2.7	1.18	0.82	0.0	2.174
HET-GCH+P_{P}	0.56	0.081	0.315	0.0037	0.020	0.09	0.21	2.4	1.06	0.70	-0.25	4.22

Table 1: Calibrated parameters of the Bastankhah and Porté-Agel wake submodel, the deflection correction model, and the Ishiahara-Qian wake-added turbulence submodel. Except for the HET-GCH+P_{P} model, the cosine exponent p_{P} was set constant and equal to 2.174 (see Fig. 2).

Depending on the implementation, the final vector of tuning parameters is obtained by stacking the respective free parameters. For the HET-GCH+P_P model, this results in:

$$\mathbf{p} = \begin{bmatrix} \mathbf{p}_W \\ \mathbf{p}_T \\ \mathbf{p}_{speed} \\ \mathbf{p}_{yaw} \end{bmatrix} . \tag{5}$$

All parameters above are identified together, resulting in a wind farm-specific simultaneous correction and tuning, which reduces the risk, driven by unmodeled physics, of adapting the baseline parameters beyond their reasonable limits. The maximum likelihood estimate of the unknown parameters $\mathbf{p}$ is obtained by minimizing the cost function

$$J(\mathbf{p}) = \frac{1}{N} \sum_{i=1}^{N} \mathbf{r}_i(\mathbf{p})^T \mathbf{R}^{-1} \mathbf{r}_i(\mathbf{p}), \tag{6}$$

where $\mathbf{r}_i(\mathbf{p})$ is the normalized vectorial difference, for a given observation i, between the measured and the FLORIS-predicted power of the three wind turbines. N is the number of observations, and $\mathbf{R}$ is the error covariance matrix. The latter is defined here as a diagonal matrix, whose entries are all equal to 0.025^2, *i.e.* the square of the expected measurement uncertainty of the normalized power [11].

The resulting optimization problem is likely ill-conditioned. Firstly, it is uncertain if all parameters are really observable given the existing measurements. And, secondly, the parameters experience probably complex couplings and interdependent sensitivities. The dilemma is overcome by assisting the identification process through a Singular Value Decomposition (SVD). The physical parameters can be mapped into a set of nonphysical but uncorrelated parameters, with which the identification is performed. At the end of the process, the parameters are rotated back into the real solution space. Further details can be found in [11].

5. Results

Half of the experimental dataset has been used for the tuning, conducted with the SVD-based parameter identification method described in Sec. 4, while the remaining half has been used for the validation. The combinations used for the parameters tuning and for the validation have been selected randomly, as shown in Fig. 4. For each implementation presented in Sec. 3.2, Table 1 reports the tuned values of the parameters of the wake models, as well as their default values (GL-default) within [7].

For each of the considered five models, Fig. 6 reports the comparison between measured data (P^{Meas}, reported on the x-axis) and corresponding predicted data (P^{FLO}, reported on the

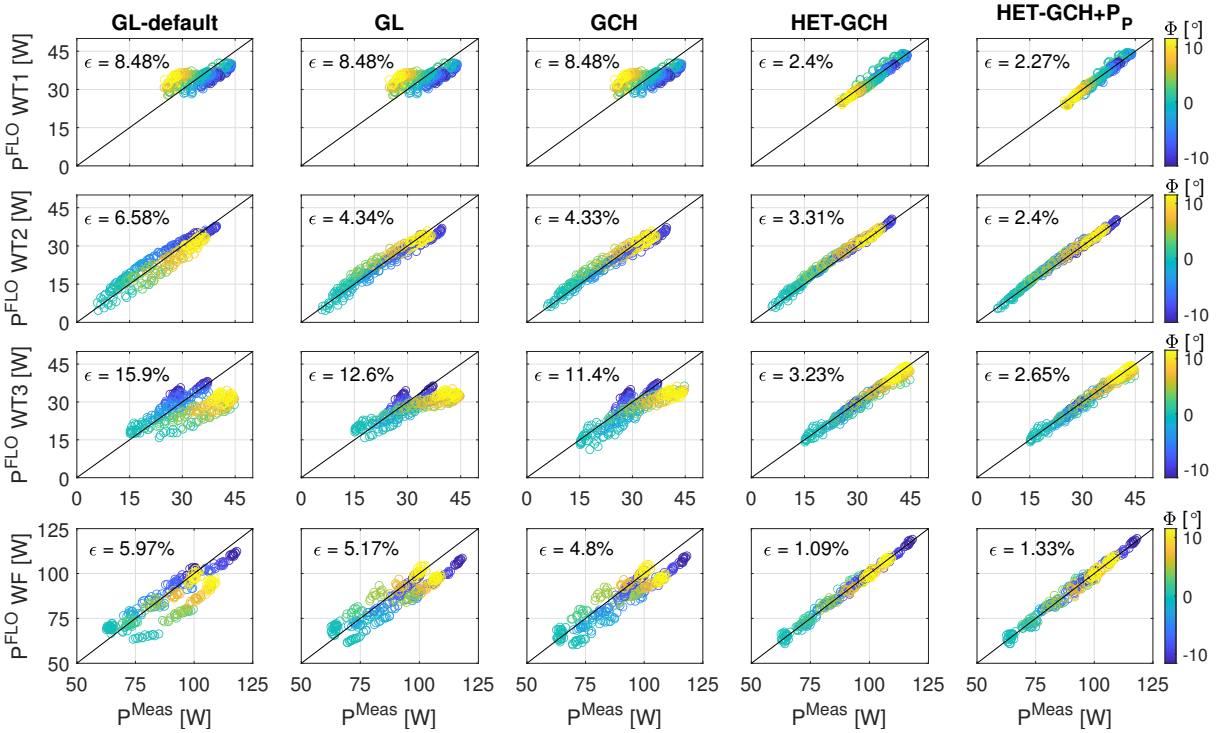

Figure 6: Comparison between measured (P^{Meas}) and predicted (P^{FLO}) power for WT1 (first row), WT2 (second row), WT3 (third row), and the entire cluster (WF, fourth row).

y-axis). Comparisons for each of the three turbines are reported in the three upper rows, while the lower one depicts the comparisons for the overall cluster (WF) power production. Within each plot, different colors are associated to different values of Φ. Finally, each subplot contains the corresponding root mean square error ϵ normalized with the rated power, equal to 46 W and 138 W respectively for the isolated wind turbine and the cluster. The following conclusions can be drawn from the analysis of Fig. 6.

- **WT1** As the GL and GCH models improve the reference implementation (GL-default) only in terms of wake related effects, they do not have any effect on the power prediction error. A significant improvement is instead noticeable when accounting for the spatial variability of the ambient wind speed. A rotation of the turntable, indeed, causes a lateral displacement of the machines located at a greater distance from the center of rotation, *i.e.* WT1 and WT3, which are therefore laterally shifted with respect to the position of the Pitot placed upstream of the cluster. As a result of the heterogeneous inflow field, the wind speed measured by the Pitot differs from the wind speed at WT1 and WT3. By considering the heterogeneity of the inflow, the power predictions for the upstream machine can thus become more accurate. For the same reason, a good match between the measured and predicted power can still be observed for the GL and GCH models with $\Phi = 0°$, *i.e.* when WT1 is immediately downstream of the Pitot. Additionally, modeling the cosine coefficient of the power law as a function of U_{REWS} further improves the predictions to some extend.
- **WT2** Being affected by the wake of WT1, the power predictions of WT2 are particularly improved even by solely calibrating the parameters of the wake submodels. As WT2 is located close to the turn-table center, its position with respect to the inflow remains relatively unchanged and immediately downstream of the Pitot tube, hence the power predictions at WT2 are less affected by accounting for the heterogeneous inflow field then

what observed for WT1. On the other side, accounting for a wind speed dependent cosine exponent allows to significantly improve the observed match.

- **WT3** The quality of the power predictions for WT3 are greatly affected by the accuracy of both the wake and the inflow field modeling. Similarly to WT1, the greatest improvement is seen after the application of a heterogeneous inflow field, with ϵ being equal to 2.65% in the HET-GCH+P_{P} implementation. It is interesting to note that modeling the effects of secondary steering (GCH model) does lead to improvements in the accuracy of the predictions, which are, nevertheless, not as significant as those observed by [11]. A possible explanation could be the modeling approach used therein, which indeed differs from the GCH one. This aspect should be the object of further investigation.
- **WF** Notwithstanding the differences observed between measurements and predictions at the single turbine level, it is very interesting to notice that, for all models, the discrepancies at the cluster level are on the whole much less. This means that, for the tested setup, over-estimations and under-estimations of the power produced at turbines level generally compensate each other. This evidence is particularly significant for the HET-GCH model, which in fact provides the most accurate predictions at the cluster level. However, when considering both the single machine and cluster predictions, the HET-GCH+P_{P} model is the most accurate. Further investigation are needed to understand if such observations may apply also to other experimental data.

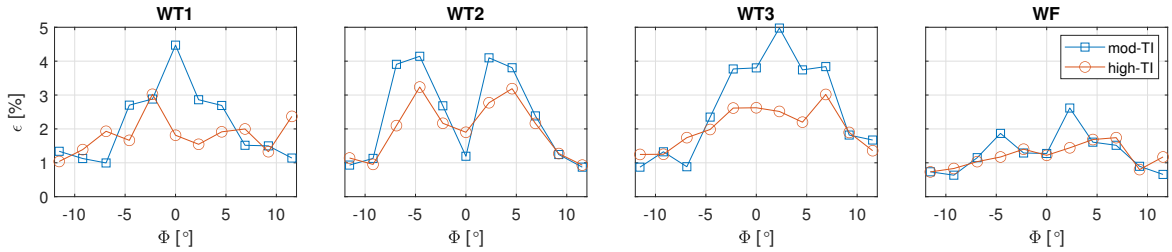

Figure 7: Distribution of ϵ for the HET-GCH+P_{P} implementation, as function of turntable angle Φ and inflow turbulence.

The prediction error for the HET-GCH+P_{P} implementation is further depicted in Fig. 7, as function of the turntable position and the inflow turbulence. Looking at all four plots, the error tends to increase for turntable angles closer to $\Phi = 0°$, *i.e.* when the downstream machines are completely immersed in the wake shed by the upstream turbines. The two peaks in the error distribution of WT2, instead, coincide with cases where WT2 is partially waked by WT1. In such a situation, WT2 is impinged by an highly in-homogeneous inflow characterized by a substantial horizontal shear, whose effects on the performance of a yawed wind turbine have shown to be significant [30], and may not be properly modeled in the considered implementations of FLORIS. Finally, the errors seem slightly higher for the mod-TI case. Under this condition, indeed, wake losses are more prominent, thus resulting that unmodeled physical effects could have a major impact on the model accuracy.

5.1. Further comments to the results

As shown in Fig 6, the application of speed-up nodes for the correction of the ambient wind speed has a considerable effect on FLORIS's power predictions. In this regard, Fig. 8 compares normalized measurements of the inflow, performed at the hub height position of WT1 and within the empty test section, to the identified inflow for the HET-GCH+P_{P} model. Specifically, the figure plots the velocity U_{REWS} predicted by the model for WT1 as its lateral position

varies due to the rotation of the turntable. Overall, there is good agreement between the measured and FLORIS modeled inflow for the high-TI case, while there exists a slight mismatch between the wind tunnel measurements and FLORIS predicted values for the mod-TI case. This discrepancy could be due to the cluster blockage, which was not accounted for in the empty chamber measurements, or even to unmodeled physics. As the speed-up nodes are identified simultaneously to the wake submodels parameters, they could indeed be tuned to values that would indirectly compensate for deficiencies in the wake model.

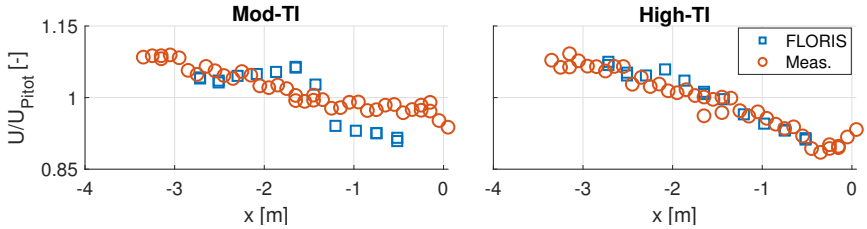

Figure 8: Measured and FLORIS predicted ambient wind speed for the HET-GCH+P_{P} model.

Regarding the coefficients k_{P} and m_{P}, it can be seen that the tuning process for the HET-GCH+P_{P} model has led to the identification of a decreasing trend of the cosine exponent P_{P} as U_{REWS} increases. This trend agrees with the shape of the power curve shown in Fig. 2a. When the G1 is misaligned, indeed, the decrease of the velocity component orthogonal to the rotor leads to a reduction of the rotation speed. As described in Sec. 2, such a reduction is coupled to a pronounced loss of efficiency of the G1 profiles, resulting in a drop in C_{P}. For low wind speeds, a misalignment of the machine therefore corresponds to a drop in its C_{P} as well. This effect produces overall a more pronounced reduction in power output under yawed conditions, and hence a higher cosine exponent P_{P}, as the wind speed decreases. This aspect is particularly critical for downstream turbines, as they are in the wake of upstream machines and thus are generally exposed to low wind speeds.

Finally, it is interesting to note how the wake submodels parameters identified for HET-GCH+P_{P} are very close to the default ones, as highlighted in Table 1. This result indicates that the default parameters can provide accurate predictions even when applied to the tested cluster of scaled machines, provided that the most relevant physical phenomena are included in the modeling.

6. Conclusions

In retrospect, it could be seen that FLORIS is able to accurately predict the output power of the tested scaled wind farm when augmented with the right correction terms, so as to increase the levels of accounted physics the simulations are built on. As a combination of the Gaussian and the Curl model, the Gauss-Curl Hybrid (GCH) implementation shows that modeling secondary steering effects does lead to better power predictions, but only a slight improvement is seen. On the other side, accounting for the inflow heterogeneity has the most significant impact on the simulation accuracy. The results showed that the application of speed-up nodes indeed reduces the error on the power predictions of the tested cluster by almost 80%. By also relating the yaw-induced power losses to the rotor-effective wind speed, the results showed a substantial improvement for the power predictions of the downstream machines, resulting in an overall wind farm error of only 1.33%.

Further research will also investigate FLORIS' ability to predict the turbulence intensity sensed by individual turbines within a cluster. For that purpose, turbulence intensity measurements derived from the standard deviation of turbine's wind speed measurements will be employed. Additionally, as the wind tunnel measurements revealed variations in turbulence

intensity and vertical shear along the lateral and longitudinal directions, further inflow correction terms will be integrated in the current implementations.

7. Acknowledgements

This work has been supported by the e-TWINS (FKZ: 03EI6020A) and the CompactWind II (FKZ: 0325492G) projects, which receives funding from the German Federal Ministry for Economic Affairs and Energy (BMWi)

References

[1] Fleming P. et al. *Renew. Energy*, 70:211 – 218, 2014.
[2] Campagnolo F. et al. *Wind Energy Sci.*, 5(4):1273–1295, 2020.
[3] Fleming P. et al. *Wind Energy Sci.*, 4(2):273–285, 2019.
[4] Fleming P. et al. *Wind Energy Sci.*, 5(3):945–958, 2020.
[5] Doekemeijer B. M. et al. *Wind Energy Sci.*, 6(1):159–176, 2021.
[6] Campagnolo F. et al. In *2020 American Control Conference (ACC)*. IEEE, 2020.
[7] NREL. Floris. version 2.3.0, 30 april 2021, 2021.
[8] Annoni J. et al. *Wind Energy Science*, 3(2):819–831, 2018.
[9] van Beek M. T. et al. *Energies*, 14(5):1293, 2021.
[10] T. Göçmen, K. Kölle, and et al. In *Journal of Physics: Conference Series*, volume 1618, 2020.
[11] Schreiber J. et al. *Wind Energy Science*, 5(2):647–673, 2020.
[12] C. L. Bottasso and F. Campagnolo. *Handb. of Wind Energy Aerodyn.*, chapter Wind Tunnel Testing of Wind Turbines and Farms. Springer, Cham, 2021.
[13] Wang C. et al. *Wind Energy Science*, 6(3):961–981, 2021.
[14] C. et al. Wang. *Wind Energy Science*, 5(4):1537–1550, 2020.
[15] NREL. Floris. version 2.4, 2021.
[16] Fleming P. et al. In *Journal of Physics: Conference Series*, volume 1618, 2020.
[17] Gebraad P. M. O. et al. *Wind Energy*, 19(1):95–114, 2016.
[18] Crespo A. and Herna J. *Journal of wind engineering and industrial aerodynamics*, 61(1):71–85, 1996.
[19] Qian G-W. and Ishihara T. *Energies*, 11(3):665, 2018.
[20] Niayifar A. and Porté-Agel F. *Energies*, 9(9):741, 2016.
[21] Bastankhah M.and Porté-Agel F. *Renewable energy*, 70:116–123, 2014.
[22] Abkar M. and Porté-Agel F. *Physics of fluids*, 27(3):035104, 2015.
[23] Bastankhah M. and Porté-Agel F. *Journal of Fluid Mechanics*, 806:506–541, 2016.
[24] Dilip D. and Porté-Agel F. *Energies*, 10(6):757, 2017.
[25] King J. et al. *Wind Energy Science*, 6(3):701–714, 2021.
[26] L. et al. Martínez-Tossas. *Wind Energy Science*, 4(1):127–138, 2019.
[27] Fleming P. et al. *Wind Energy Science*, 3(1):243–255, 2018.
[28] Segalini et al. Blockage effects in wind farms. *Wind Energy*, 23(2):120–128, 2020.
[29] Simley E. et al. *Wind Energy Science*, 6(6):1427–1453, 2021.
[30] Howland M. et al. *Journal of Renewable and Sustainable Energy*, 12(6):063307, 2020.